Peripheral Defocus of the Monkey Crystalline Lens With Accommodation in a Lens Stretcher

Bianca Maceo Heilman,[1,2] Fabrice Manns,[1,2] Marco Ruggeri,[1] Arthur Ho,[1,3,4] Alex Gonzalez,[1] Cor Rowaan,[1] Andres Bernal,[5] Esdras Arrieta,[1] and Jean-Marie Parel[1,2,6]

[1]Ophthalmic Biophysics Center, Bascom Palmer Eye Institute, Miami, Florida, United States
[2]Biomedical Optics and Laser Laboratory, Department of Biomedical Engineering, University of Miami College of Engineering, Coral Gables, Florida, United States
[3]Brien Holden Vision Institute, Sydney, New South Wales, Australia
[4]School of Optometry and Vision Science, University of New South Wales, Australia
[5]Bioniko Consulting LLC, Sunny Isles Beach, Florida, United States
[6]Vision Cooperative Research Centre, Sydney, New South Wales, Australia

Correspondence: Fabrice Manns, Bascom Palmer Eye Institute, 1638 NW 10 Avenue, Miami, FL 33136, USA;
fmanns@miami.edu.

Submitted: November 1, 2017
Accepted: March 14, 2018

Citation: Maceo Heilman B, Manns F, Ruggeri M, et al. Peripheral defocus of the monkey crystalline lens with accommodation in a lens stretcher. *Invest Ophthalmol Vis Sci*. 2018;59:2177–2186. https://doi.org/10.1167/iovs.17-23273

Purpose. To characterize the peripheral defocus of the monkey crystalline lens and its changes with accommodation.

Methods. Experiments were performed on 15 lenses from 11 cynomolgus monkey eyes (age: 3.8–12.4 years, postmortem time: 33.5 ± 15.3 hours). The tissue was mounted in a motorized lens stretcher to allow for measurements of the lens in the accommodated (unstretched) and unaccommodated (stretched) states. A custom-built combined laser ray tracing and optical coherence tomography system was used to measure the paraxial on-axis and off-axis lens power for delivery angles ranging from −20° to +20° (in air). For each delivery angle, peripheral defocus was quantified as the difference between paraxial off-axis and on-axis power. The peripheral defocus of the lens was compared in the unstretched and stretched states.

Results. On average, the paraxial on-axis lens power was 52.0 ± 3.4 D in the unstretched state and 32.5 ± 5.1 D in the stretched state. In both states, the lens power increased with increasing delivery angle. From 0° to +20°, the relative peripheral lens power increased by 10.7 ± 1.4 D in the unstretched state and 7.5 ± 1.6 D in the stretched state. The change in field curvature with accommodation was statistically significant ($P < 0.001$), indicating that the unstretched (accommodated) lens has greater curvature or relative peripheral power.

Conclusions. The cynomolgus monkey lens has significant accommodation-dependent curvature of field, which suggests that the lens asserts a significant contribution to the peripheral optical performance of the eye that also varies with the state of accommodation.

Keywords: crystalline lens, laser ray tracing, peripheral defocus, accommodation

The optics related to the periphery of the visual field, including peripheral refraction and off-axis aberrations, are associated with refractive error.[1–4] Previous studies suggest that peripheral refraction may be a factor in the onset and progression of myopia in humans,[3–7] although there is disagreement in the literature regarding the role of peripheral defocus in myopia in human eyes.[8–10] As a result, peripheral optical treatment strategies have been recently proposed as a method for correcting and slowing the progression of myopia, and short-term clinical results have demonstrated some measurable efficacy.[5] The primary goal of peripheral treatment strategies is to decrease the relative hyperopic defocus across the visual field.[4]

Despite its importance to ocular growth and myopia development, the factors that contribute to peripheral defocus and its changes during refractive development and with age[11] are not yet well established. It is well known that the crystalline lens power and aberrations change significantly with age[12–16] due to the continuous growth of the lens. In addition, studies have shown that peripheral refraction may be influenced by accommodation.[17–20] It is therefore likely that changes in the optics of the crystalline lens contribute to the changes in the peripheral optics of the whole eye.

It is challenging to directly characterize the peripheral defocus of the in vivo crystalline lens due to the lens' position behind the cornea and iris. Ex vivo lens stretching systems[12,21–23] have enabled the direct measurement of lens power, aberrations, and shape during simulated accommodation, but to the best of our knowledge, there have been no studies on the dependence of isolated lens power on incidence angle. This information is key to understanding the optics of the lens in the peripheral field. The purpose of this study was to characterize the peripheral defocus of the crystalline lens and its changes with accommodation using a new instrument that enables off-axis power measurements of the lens mounted in a lens stretcher.

Methods

Monkey Tissue

Data were acquired on 15 lenses from 11 cynomolgus monkeys obtained from the division of veterinary resources at the

University of Miami as part of a tissue-sharing protocol (*Macaca fascicularis*, age: 3.8–12.4 years, postmortem time: 33.5 ± 15.3 hours). Experiments were performed on the lenses using a custom-built combined laser ray tracing (LRT) and optical coherence tomography (OCT) system (Figs. 1A, 1B) to measure the paraxial on-axis and off-axis power of the lens. All experiments adhered to the ARVO Statement for the Use of Animals in Ophthalmic and Visual Research and to the University of Miami's Institutional Animal Care and Use Guidelines. No animals were euthanized for the sole purpose of this study. The eyes were enucleated immediately after euthanasia, wrapped in wet gauze, and stored in an air-tight container. Upon arrival at the laboratory, all eyes were either prepared for experiments or refrigerated at 4°C.

Tissue Preparation

The tissue dissection followed the protocol described in Nankivil et al.[23] To summarize, the whole globe was bonded to eight scleral shoes. Next, the posterior pole, the cornea, and iris were removed, and incisions were made in between the sclera of adjacent shoes to create eight independent segments for stretching. The crystalline lens was carefully inspected to ensure that the lens was transparent and free of signs of cataract or lens capsule delamination. The tissue was then mounted in a custom-built miniature motorized lens stretching apparatus (STR-MLS-B, basic lens stretcher; Bioniko Consulting LLC, Sunny Isles Beach, FL, USA) that simulates disaccommodation by displacing the shoes outward (Fig. 1C). Maximum stretch of the tissue is 5.25 mm in diameter and the precision of the stretching positions is within ±0.05 mm.

The lens stretcher was placed in a custom chamber with a built-in miniature servomotor (HS-5055, Servo City, Winfield, KS, USA) and gears, which enable automated stretching of the tissue. The bottom of the chamber is a 1-mm thick sapphire window (45-568; Edmund Optics, Barrington, NJ, USA). The tissue chamber is placed on an aluminum holder mounted on a three-axis translation stage (460A-X & 460A-XY; Newport Corp., Irvine, CA, USA) enabling precise centration and axial positioning of the lens within the LRT-OCT system (Fig. 1A). In all experiments, the tissue chamber was filled with balanced salt solution (BSS, Alcon Inc., Ft. Worth, TX, USA) to ensure that the lens stretcher was fully submersed and the tissue remained hydrated throughout the experiment. The fluid was injected slowly near the chamber wall and away from the lens using a 30-mL syringe and needle to ensure that no air bubbles were formed. The same fluid level was used for all experiments.

LRT-OCT System Description

A basic schematic of the combined LRT and OCT system depicting the off-axis data acquisition is shown in Figure 1D. The system is based on a previous setup,[16] which has been enhanced to enable off-axis three-dimensional (3D) OCT imaging of the crystalline lens and acquisition of two-dimensional (2D) LRT data for wavefront reconstruction with lens stretching.

The OCT system (ENVISU R4400; Bioptigen/Leica Microsystems, Morrisville, NC, USA) acquires images at 880 nm with a depth range of 16 mm and axial resolution of 8 μm in air (Fig. 1B). The OCT system was coupled to a custom-built telecentric beam delivery system[24] with a 100-mm focal length in order to image the crystalline lens. The same beam delivery probe is used to acquire the LRT data. For optimal OCT image quality, the focal plane of the scanning beam is positioned near the center of the crystalline lens during imaging. OCT images are used to center and align the crystalline lens for LRT experiments. The custom delivery probe is mounted on a motorized rotation stage (T-RS60A; Zaber Technologies, Vancouver, BC) that pivots around the crystalline lens to allow acquisition of off-axis spot patterns.

To acquire the ray trace data, a high-resolution CMOS digital image sensor (DCC1545M-GL, Thorlabs, Newton, NJ, USA) is mounted below the lens on a 2D (horizontal and vertical) motorized positioning stage (T-LSR150B and T-LSR075B; Zaber Technologies, Vancouver, BC). This image sensor is used to record spot positions, corresponding to the cross-section of the laser beam, at multiple heights below the lens. The spot positions are used to calculate the slope of each ray exiting the lens, enabling measurement and calculation of the lens power. The LRT data acquisition was fully automated via custom LabView (National Instruments Corp., Austin, TX, USA) software.

Experimental Procedure

The tissue chamber containing the lens stretcher was placed in the system and live images were acquired with the OCT system to align and center the crystalline lens. The axial position of the tissue chamber was adjusted so that the center of the lens was placed at the pivot point of the rotation stage (Fig. 2). This ensures that the chief rays for the varying delivery angles intersect at the center of the lens. Once the crystalline lens was properly positioned in the system, LRT experiments were performed on the lens in the unstretched state. The LRT system was programmed to automatically perform a meridional ray trace by sequentially delivering 27 equally spaced parallel rays (0.21 mm spacing) along one meridian of the crystalline lens.

At the beginning of the experiment, the camera was positioned at a height 1 mm below the tissue chamber, and the camera was shifted horizontally until the spot corresponding to the central ray was detected. Once the ray was detected, the horizontal position was recorded and the scanning sequence commenced; 27 rays were delivered sequentially along the lens and the spot image corresponding to each individual ray was recorded. Following the completion of the image acquisition, the height of the camera was moved downward to the next axial position, the horizontal position of the camera was moved until the spot corresponding to the central ray was detected, and the scanning sequence was repeated at the next camera height. Spot images were acquired along the optical axis for vertical positions ranging up to 24 mm with an axial increment of 1 or 2 mm.

LRT data was acquired at delivery angles ranging from −20° to +20°. Data for the first four lenses were acquired in 5° increments. In later experiments, the scanning increment was adjusted to 2° for angles less than 10° and 5° for angles greater than 10° to enable more precise measurements of the angular dependence near the axis. Thus, the delivery angles for the subsequent experiments corresponded to: ±20°, ±15°, ±10°, ±8°, ±6°, ±4°, ±2°, and 0°. The precision of the angle delivery was estimated to be 0.14°. It is important to note that the delivery angle refers to the angle that the laser beam is delivered in air. The angle of incidence on the lens is lower, 0.74 to 0.75 times the delivery angle, due to refraction of the beam at the air to BSS fluid interface.

Following the completion of the unstretched lens experiment, the tissue was stretched to the 5.25 mm position. The tissue alignment protocol was repeated, and the LRT experiment was performed on the lens in the stretched state.

Data Analysis

The method used to calculate lens power has been described in a previous publication.[16] In summary, a

Investigative Ophthalmology & Visual Science

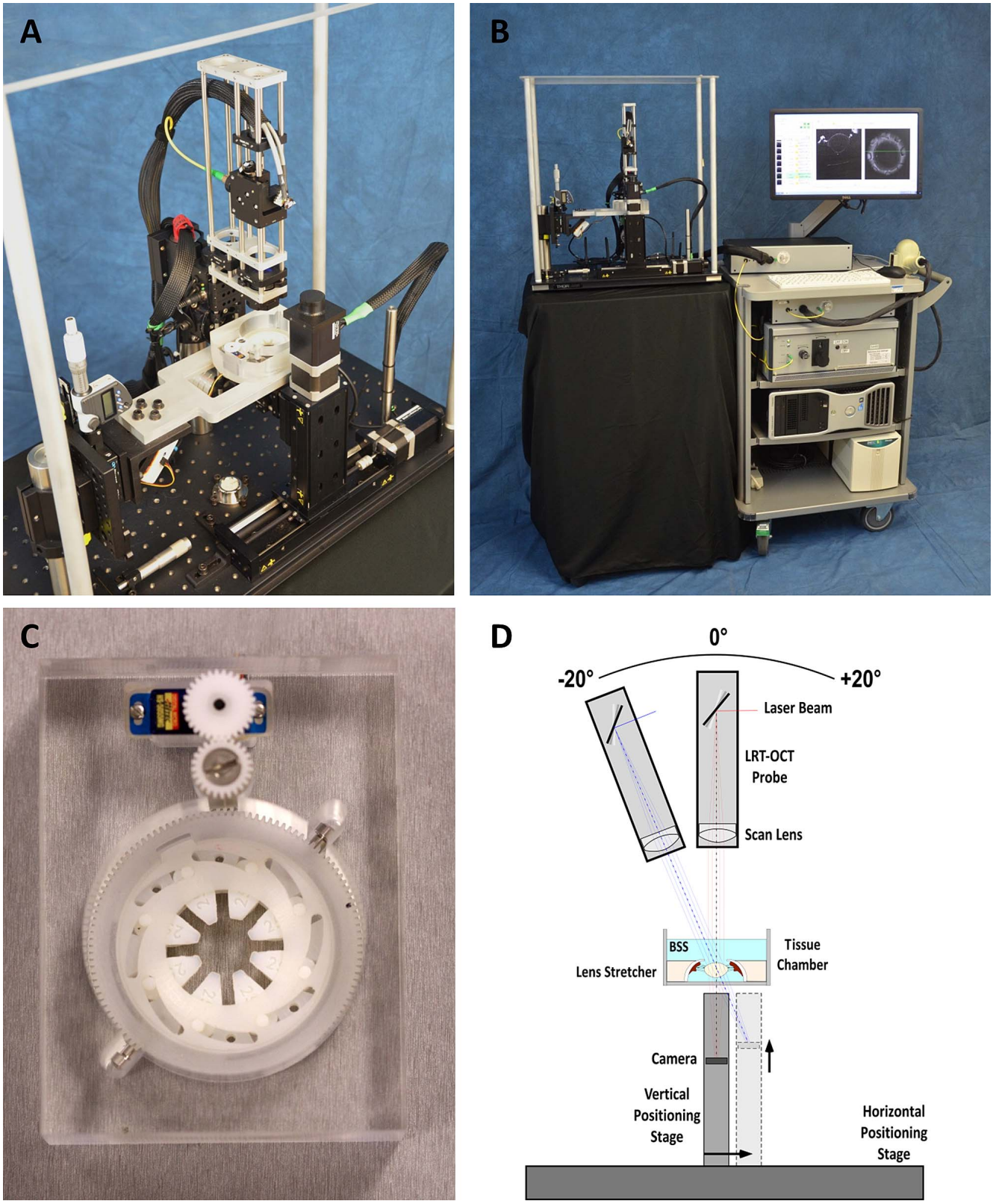

Figure 1. (**A**) Close-up of the LRT system setup. (**B**) The combined LRT and OCT system. (**C**) Lens stretcher used for automated stretching of the ocular tissue mounted in the tissue chamber. (**D**) LRT-OCT system schematic demonstrating the principle of off-axis LRT data acquisition. The probe rotates about the crystalline lens and a camera mounted on a 2D motorized positioning stage located below the tissue chamber is used to record the spot positions along each individual ray for all delivery angles.

Investigative Ophthalmology & Visual Science

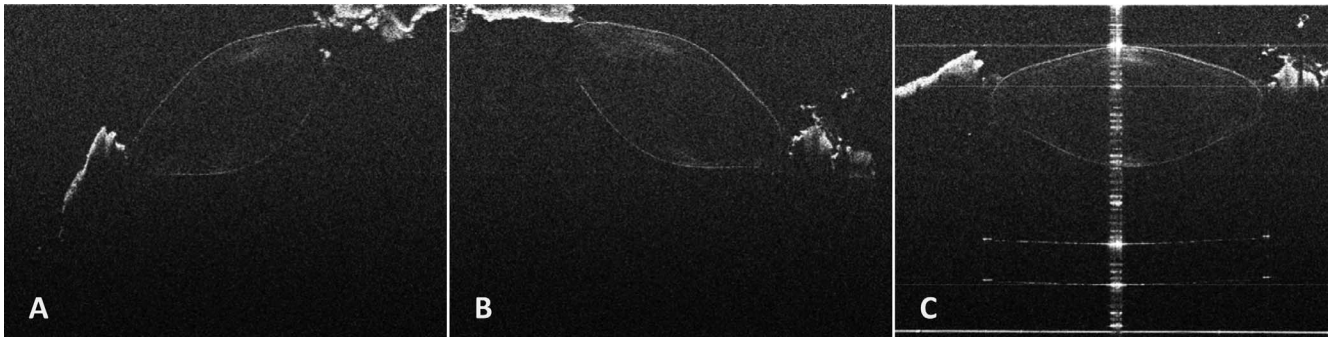

Figure 2. OCT images of an unstretched cynomolgus monkey lens (age: 5.7 years, postmortem time: 24 hours) used to align and center the crystalline lens in the LRT-OCT system. Images were acquired at (**A**) −45°, (**B**) +45°, and (**C**) 0° delivery angles. The axial adjustment was performed by rotating the delivery probe to the −45° and +45° positions, and modifying the height of the tissue chamber until the lens remained centered in the OCT scans when the rotation stage was switched between the two positions. When this condition was satisfied, the lens was located at the pivot point of the rotation stage.

computing program (MATLAB R2015b; MathWorks, Inc., Natick, MA, USA) was used to calculate the centroid of each spot for all the images. The centroid position was used as an estimate for the ray height incident on the camera. For each axial position, the estimated ray height was plotted as a function of entrance ray height, and fit with a third-order polynomial. A linear regression of the axial dependence of the first-order coefficients of these fits provides the distance between the image principal plane of the lens and the axial position where the LRT rays intersect the chief ray in paraxial approximation. The coefficients of the linear regression were used to calculate the effective optical power, P (diopter [D]), of the crystalline lens for each delivery angle, α. The change in lens power, or relative peripheral lens power, from the on-axis (0°) position was calculated for each respective angle, where

$$\Delta P = P(\alpha) - P(0^{\circ}) \quad (1)$$

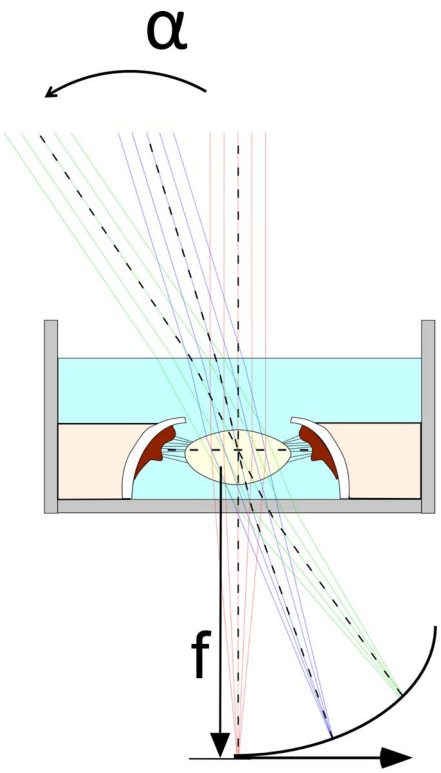

Figure 3. Basic schematic depicting the rays entering the crystalline lens at varying delivery angles, α. The rays pass through the lens and are focused in the image plane at the lens focal point, f.

Figure 3 shows a basic schematic of the rays entering the crystalline lens at varying delivery angles and being focused in the image plane. The change in lens power, or peripheral defocus, was calculated for lenses in the unstretched and stretched states. The peripheral defocus was plotted with respect to delivery angle for all of the lenses, and a repeated measures ANOVA was used to compare the relative peripheral lens power in the unstretched and stretched states.

The radius of curvature of the image field was calculated by performing a second degree polynomial curve fit of the variation of the axial coordinates (z) of the ray intersection points as a function of the lateral coordinate (y) for delivery angles ranging from −20° to +20°. In first-order approximation, the radius of curvature (R) is proportional to the second-degree coefficient (a) of the polynomial ($R = 1/[2a]$). This curvature is the tangential field curvature.

Results

Figure 4 (left) shows a basic schematic of the spot image acquisition where discrete points along each individual ray are captured with an imaging sensor. The measured spot positions with respect to camera height exhibit a linear trend and the central rays appear to converge at the focal point of the lens. The spot position versus camera height for the individual rays at the 0° and 20° delivery angles are plotted for an unstretched cynomolgus monkey lens in Figure 4 (center, right). Representative results acquired with the LRT-OCT system are shown in Figure 5, including a graph of the change in lens power versus delivery angle and OCT images of the lens acquired at varying delivery angles. Graphs demonstrating the variation of power with delivery angle for lenses in the unstretched and stretched states are shown for the youngest (Fig. 6) and oldest (Fig. 7) monkey lenses in this study.

In the case where measurements were obtained on both lenses from the same monkey, one lens was randomly selected to be included in the statistical analysis for this study and the other was excluded to account for the correlation between eyes.[25] Table 1 shows the cynomolgus monkey lens power in the unstretched and stretched states with respect to delivery angle for all of the lenses in this study. The lenses that were excluded from the analysis are indicated with an asterisk. On average, the on-axis effective lens power was 52.0 ± 3.4 D for lenses in the unstretched state and 32.5 ± 5.1 D in the

Investigative Ophthalmology & Visual Science

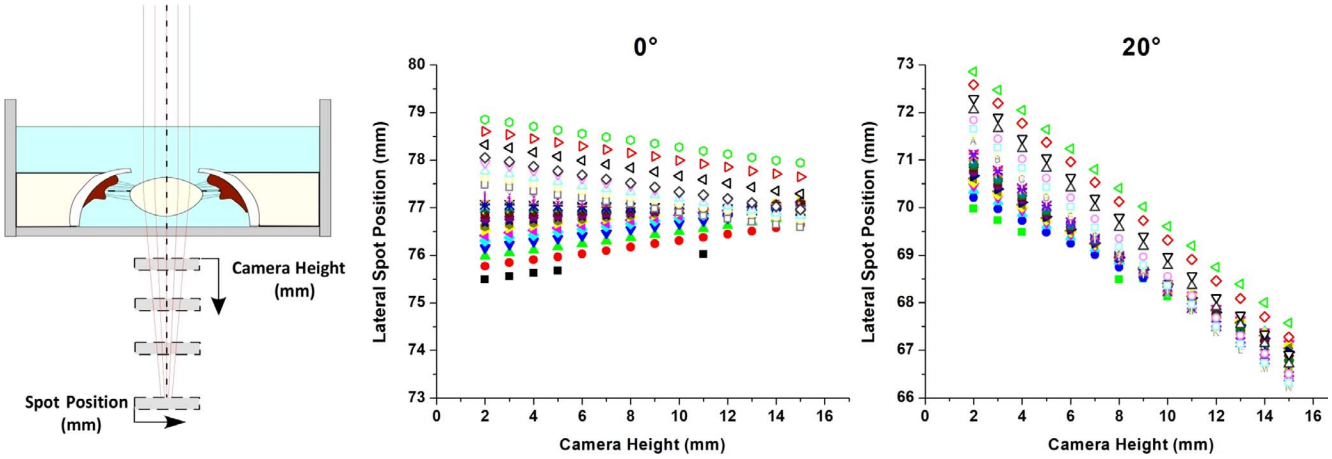

FIGURE 4. (*Left*) Basic schematic of spot image acquisition. Discrete points along each ray are captured with the imaging sensor shown at 0° (*center*) and (*right*) 20° delivery angles for a typical stretched cynomolgus monkey lens (age: 6.3 years, postmortem time: 24 hours). The spot positions correspond to the lateral position of the camera (in mm) on the horizontal positioning stage and the camera height (in mm) is the position of the camera on the vertical positioning stage (where 0 mm is the highest position of the stage and the camera is translating downward and away from the crystalline lens). The spot positions vary based on the delivery angle.

stretched state. The accommodative range of the lenses, calculated as the difference between the unstretched and stretched lens power, is shown for each of the delivery angles in Table 2.

Table 3 shows the relative peripheral lens power with respect to delivery angle for the unstretched and stretched lenses. The peripheral defocus of the lens was found to increase significantly with increasing delivery angle, with an average increase from 0° to +20° of 10.7 ± 1.4 D in the unstretched state and 7.5 ± 1.6 D in the stretched state. The corresponding tangential radius of curvature of the image field was −6.7 ± 0.8 mm in the unstretched state and −9.2 ± 1.3 mm in the stretched state.

A planned analysis in the form of a repeated measures ANOVA was performed on the relative peripheral lens power (peripheral minus central) with linear and quadratic trends as within-subject factors and the contrasts representing linear (tilt) and quadratic (curvature) trends in the data. Three pairs of linear and quadratic trends were used to test the effects of accommodation on the lens field curvature: the unstretched results, the stretched results, and the difference (unstretched versus stretched interaction). In two cases, the peripheral lens power could not be measured at the +20° position. In order for the contribution of the two cases with missing values to be equivalent to the other cases, a set of linear and quadratic contrast coefficients were calculated to take into the account

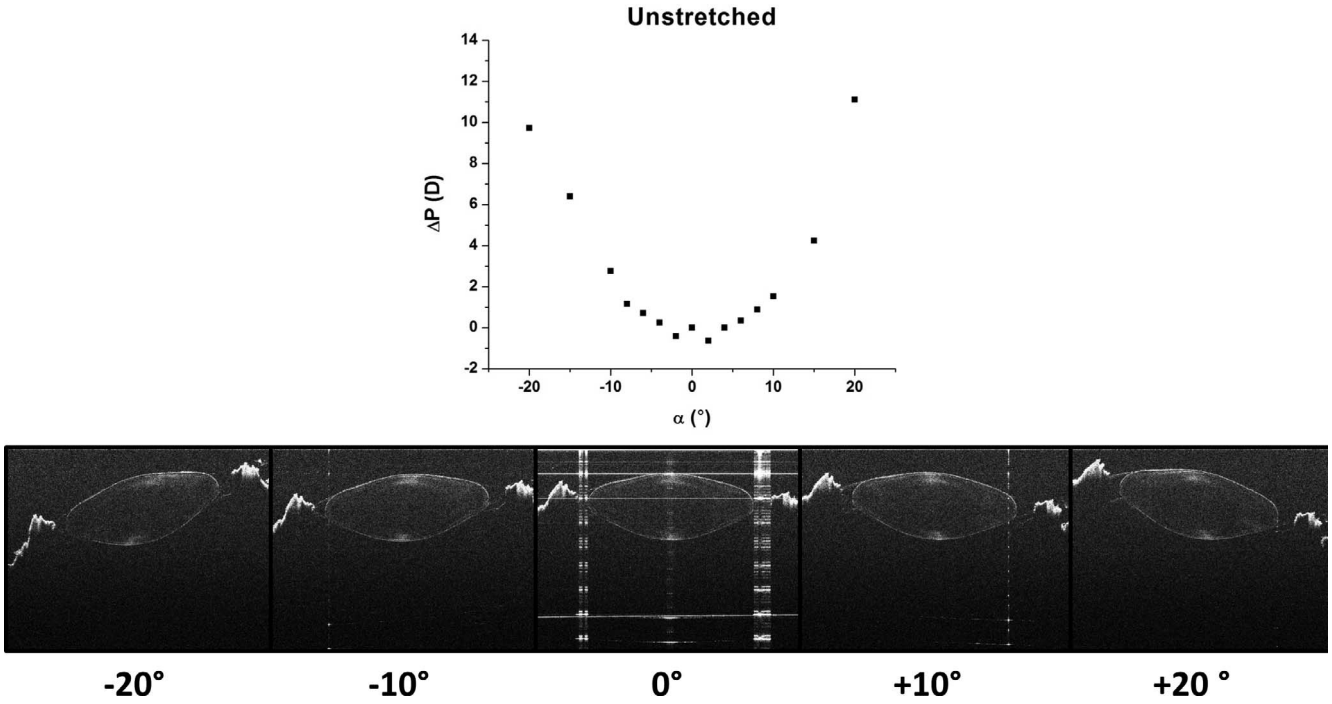

FIGURE 5. Typical results for an LRT-OCT experiment. *Top*: graph depicting the change in lens power (*P*) versus delivery angle (α) for an unstretched cynomolgus monkey lens (age: 9.2 years, postmortem time: 24 hours). *Bottom*: sample OCT images of the crystalline lens acquired at delivery angles ranging from −20° to +20°, the same projection angles that the LRT scans were performed.

Investigative Ophthalmology & Visual Science

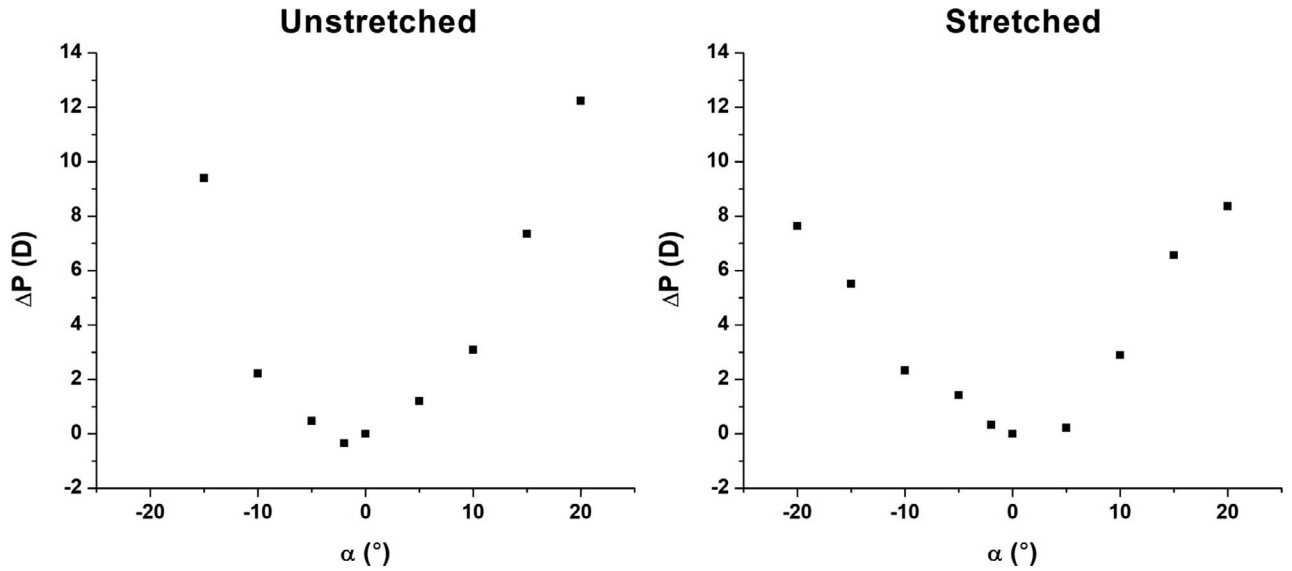

FIGURE 6. The change in lens power (*P*) with respect to delivery angle (α) for the youngest cynomolgus monkey lens (age: 3.8 years, postmortem time: 22 hours) in the unstretched (*left*) and stretched (*right*) states.

the missing values. The *P* values were all greater than 0.40 for the linear trends and linear interaction contrasts; thus, the linear trend (corresponding to tilt of the wavefront) in peripheral power with respect to delivery angle for the unstretched and stretched lenses was not statistically significant. Furthermore, there is no significant difference in tilt between the two states.

All of the *P* values for the quadratic trends had a decision-wise Type I probability of less than 0.001, indicating there is statistically significant curvature of field in both the unstretched and stretched lenses with increasing positive power toward the periphery. The change in field curvature with accommodation was statistically significant ($P < 0.001$), indicating that the unstretched (accommodated) lens has greater curvature or relative peripheral power. These findings for solely the crystalline lens are qualitatively similar to the results obtained on in vivo human eyes.[17,18]

The on-axis and off-axis power of the lens appeared to decrease slightly with age. However, this trend was not statistically significant. The results for the relative peripheral lens power were independent of age for the unstretched and stretched lenses.

Discussion

A new method was used to directly measure changes in the lens off-axis power during simulated accommodation in a motorized lens stretcher. This study demonstrates the feasibility of acquiring precise on-axis and off-axis ray trace measurements of the crystalline lens using a combined LRT-

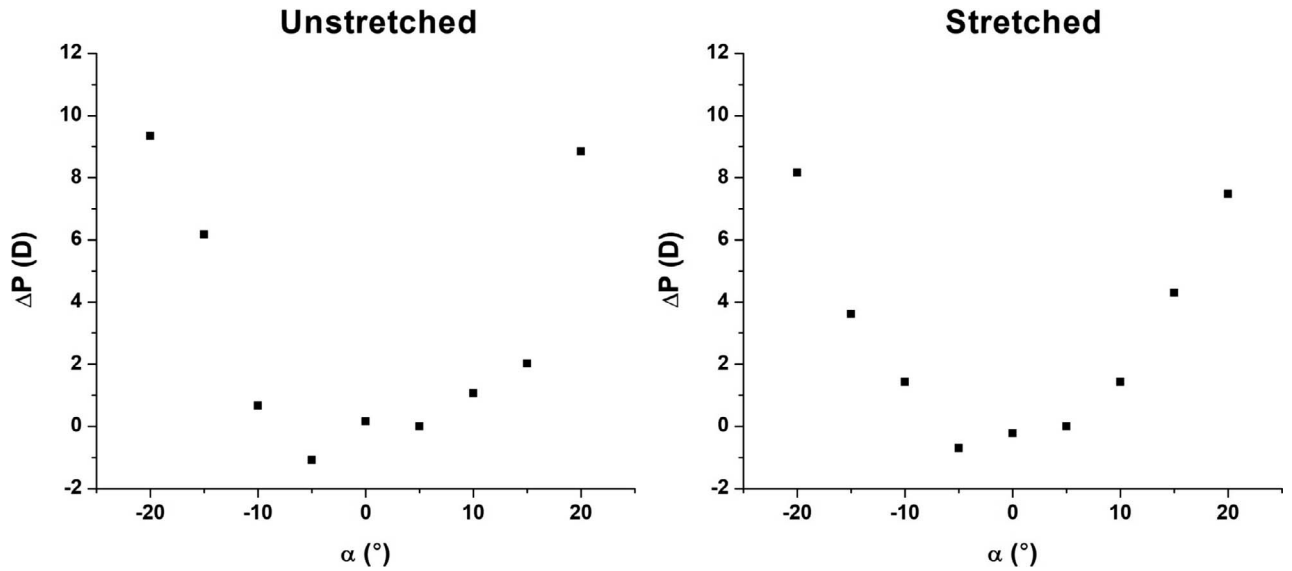

FIGURE 7. The change in lens power versus delivery angle for an older cynomolgus monkey lens (age: 12.4 years, postmortem time: 24 hours) in the unstretched (*left*) and stretched (*right*) states.

Investigative Ophthalmology & Visual Science

Table 1. Cynomolgus Monkey Lens Power (D) Measured for the Delivery Angles: ±20°, ±15°, ±10°, ±5°, 0°

		Unstretched Lens Power, D								
Eye No.	**Age, y**	**−20°**	**−15°**	**−10°**	**−5°**	**0°**	**5°**	**10°**	**15°**	**20°**
1 OD	3.8	NA	61.5	54.3	52.6†	52.1	53.9†	55.2	59.5	64.4
2 OD	5.7	70.9	65.5	61.7	59.7†	58.6	58.9†	60.9	63.4	69.2
3 OD	6.3	65.5	65.0	50.3	55.6	54.0	53.3	50.3	55.8	65.5
3 OS*	6.3	66.7	59.3	57.4	55.4	53.9	54.8	56.8	58.9	63.9
4 OD*	6.8	65.8	61.9	63.5	54.6	57.4	56.2	56.9	62.1	67.4
4 OS	6.8	63.9	61.9	55.5	54.1	54.6	54.8	56.3	61.4	66.4
5 OD	7.8	64.3	59.5	57.0	56.9	54.7	54.7	57.6	59.5	65.8
6 OD	8.4	65.5	58.4	51.8	52.5†	52.3	48.9†	54.8	56.1	60.2
7 OS	8.5	63.1	57.4	53.9	53.8	51.9	54.0	57.2	60.5	63.5
8 OD	9.2	59.6	56.3	52.6	50.1†	49.9	49.9†	51.4	54.1	61.0
9 OD	10.6	58.3	53.2	47.8	48.2	47.7	48.9	49.6	54.4	56.8
9 OS*	10.6	56.3	51.1	48.3	46.7†	45.6	50.2†	50.3	52.6	54.8
10 OD	12.4	56.7	52.7	50.9	48.1†	48.4	49.3†	50.0	52.5	60.0
11 OD*	12.4	58.9	50.9	48.8	52.0	50.6	50.4	48.8	51.9	57.1
11 OS	12.4	56.7	53.5	48.0	46.2	47.5	47.3	48.4	49.3	56.2
Average		62.4	58.6	53.1	52.5	52.0	52.2	53.8	57.0	62.6
SD		4.6	4.5	4.1	4.1	3.4	3.5	4.1	4.3	4.1
		Stretched Lens Power, D								
Eye No.	**Age, y**	**−20°**	**−15°**	**−10°**	**−5°**	**0°**	**5°**	**10°**	**15°**	**20°**
1 OD	3.8	41.4	39.2	36.1	35.2†	33.7	34.0†	36.6	40.3	42.1
2 OD	5.7	48.6	44.6	41.5	40.2†	38.8	39.1†	41.0	42.6	46.8
3 OD	6.3	41.2	35.0	32.1	32.5	34.0	32.4	37.3	37.9	39.8
3 OS*	6.3	52.1	47.4	44.2	41.9	43.1	45.0	44.9	46.2	53.6
4 OD*	6.8	45.8	44.1	39.9	39.1	40.3	38.4	41.2	44.6	45.9
4 OS	6.8	40.9	36.9	34.8	33.1	34.5	32.0	35.8	38.6	43.7
5 OD	7.8	39.7	36.1	33.3	30.8	31.7	32.3	32.3	35.7	39.3
6 OD	8.4	39.9	33.0	30.5	30.7†	31.5	28.8†	32.2	30.0	39.1
7 OS	8.5	NA	46.5	46.6	42.9	43.1	42.5	44.6	48.6	53.1
8 OD	9.2	33.7	31.8	29.0	27.5†	27.0	28.2†	29.0	31.4	34.8
9 OD	10.6	33.2	28.8	28.9	26.7	26.9	26.7	25.7	29.3	33.0
9 OS*	10.6	36.6	31.8	30.1	27.4†	26.5	26.9†	27.4	28.7	31.3
10 OD	12.4	32.2	29.0	25.8	25.0†	27.6	24.5†	26.4	28.0	31.8
11 OD*	12.4	36.2	34.2	30.6	28.3	28.6	28.0	29.7	31.2	34.5
11 OS	12.4	37.4	32.8	30.6	28.5	29.0	29.2	30.6	33.5	36.7
Average		38.8	35.8	33.6	32.1	32.5	31.8	33.8	36.0	40.0
SD		4.9	5.8	6.0	5.6	5.1	5.3	5.9	6.3	6.3

Measurements were obtained for each lens in the unstretched and stretched states.
* Eyes shown in the Table but were excluded for the statistical analysis.
† Lens power measurement corresponds to the ±4° delivery angle rather than ±5°.

OCT system. Our results show that the cynomolgus monkey lens has significant curvature of field in the accommodated (unstretched) and unaccommodated (stretched) states. Lens power was found to significantly increase peripherally with increasing delivery angle in the unstretched and stretched states for all lenses, corresponding to myopic peripheral defocus. Furthermore, the peripheral defocus of the monkey lens was found to significantly increase with accommodation.

The values of peripheral defocus provided by the LRT-OCT system cannot be directly compared to the peripheral defocus obtained in vivo from the measurement of peripheral refraction for several reasons. First, the system measures defocus in the plane that would correspond to the retinal image plane in vivo referenced with respect to the back principal plane of the lens, whereas the peripheral defocus obtained from in vivo refraction is quantified with respect to the position of the axial conjugate of the retina referenced to the spectacle or corneal plane. Second, the LRT-OCT system measures lens field curvature relative to a flat image plane (CMOS sensor). Third, it provides the peripheral defocus for the crystalline lens isolated from the optical system of the eye. The measurements are acquired with parallel rays incident on the lens, whereas in vivo, the rays incident on the lens have been focused by the cornea. According to the theory of third-order aberrations[26] for a thin lens with the aperture stop in the plane of the lens, field curvature is independent of input object vergence and depends only on the refractive indices of the lens material and surrounding media and on the radii of curvature of the lens surfaces. We therefore do not expect that object vergence has a significant effect on our findings.

This is the first system capable of acquiring direct measurements of the ex vivo lens peripheral defocus and its changes with simulated accommodation. Previous systems[12,14–15] estimated the on-axis lens power, but were subject to measurement error due to the difficulty in quantifying the path of the paraxial rays. A key advantage of the LRT-OCT system is its ability to directly measure the individual slopes of

Investigative Ophthalmology & Visual Science

Table 2. The Accommodative Range Calculated as the Difference Between Unstretched and Stretched Lens Power for the Delivery Angles: ±20°, ±15°, ±10°, ±5°, 0°

		Unstretched – Stretched Lens Power, D								
Eye No.	**Age, y**	**−20°**	**−15°**	**−10°**	**−5°**	**0°**	**5°**	**10°**	**15°**	**20°**
1 OD	3.8	NA	22.3	18.3	17.4†	18.4	19.9†	18.6	19.2	22.3
2 OD	5.7	22.3	20.9	20.2	19.5†	19.8	19.8†	19.9	20.8	22.4
3 OD	6.3	24.3	30.0	18.2	23.1	20.0	20.9	13.0	17.9	25.7
3 OS*	6.3	14.6	11.9	13.2	13.5	10.8	9.8	11.9	12.7	10.3
4 OD*	6.8	20.0	17.8	23.6	15.5	17.1	17.8	15.7	17.5	21.5
4 OS	6.8	23.0	25.0	20.7	21.1	20.0	22.8	20.5	22.8	22.6
5 OD	7.8	24.6	23.4	23.7	26.1	23.0	22.4	25.3	23.9	26.5
6 OD	8.4	25.5	25.4	21.4	21.9†	20.8	20.2†	22.6	26.1	21.1
7 OS	8.5	NA	10.9	7.2	10.8	8.7	11.6	12.5	11.9	10.4
8 OD	9.2	25.9	24.5	23.6	22.6†	22.9	21.7†	22.4	22.7	26.1
9 OD	10.6	25.1	24.4	18.9	21.5	20.8	22.2	23.9	25.1	23.8
9 OS*	10.6	19.8	19.4	18.2	19.3†	19.1	23.3†	22.9	23.8	23.5
10 OD	12.4	24.5	23.7	25.1	23.1†	20.7	24.8†	23.6	24.4	28.2
11 OD*	12.4	22.7	16.7	18.2	23.6	22.0	22.4	19.1	20.7	22.5
11 OS	12.4	19.3	20.7	17.4	17.7	18.5	18.1	17.7	15.8	19.5
Average		23.8	22.8	19.5	20.4	19.4	20.4	20.0	21.0	22.6
SD		2.0	4.7	4.8	4.0	3.8	3.4	4.3	4.4	4.8

* Eyes shown in the Table 2, but were excluded for the statistical analysis.
† Lens power measurement corresponds to the ±4° delivery angle rather than ±5°.

the rays exiting the crystalline using an imaging sensor mounted on a 2D motorized positioning stage. The system is capable of measuring the off-axis power of the lens and the experiment is completely automated.

We used the delivery angle in air as a reference instead of the incidence angle in aqueous medium to enable a closer comparison with the in vivo peripheral field angle. A ray-tracing analysis comparing the LRT-OCT system and the Navarro eye model[27] shows that for a 20° field angle in air, the angle of the chief ray on the lens is 3° less in the LRT system than in the eye model. Within the angular range of our measurements, and for a given incidence angle on the lens, the delivery angle in air for the LRT-OCT system therefore approximately corresponds to the in vivo peripheral field angle.

The radius of curvature of the tangential image field corresponding to the measured peripheral defocus can provide some insight into potential visual implications. On average, the radius of curvature of the tangential image field was -6.8 ± 0.8 mm for the unstretched lens and -9.2 ± 1.3 mm for the stretched lens, and the diameter of the cynomolgus monkey globe is on the order of 19 mm.[28] The field curvature of the stretched lens therefore matches approximately the expected radius of curvature of the retina (9.5 mm). However, the increased field curvature of the unstretched lens suggests that accommodation will introduce significant peripheral myopic defocus in cynomolgus monkeys.

The lens peripheral defocus could be due to the surface shape or to the lens gradient refractive index. In order to determine whether the lens gradient refractive index contributes to the peripheral defocus of the lens, we compared our experimental data with the peripheral defocus of a homogeneous lens simulated in a ray-tracing software (OSLO, Lambda Research Corp, Littleton, MA, USA). The values for the lens shape and equivalent refractive index were assumed for a typical 6-year-old cynomolgus monkey lens (anterior lens radius = 4.02 mm, posterior lens radius = -3.34 mm, lens thickness = 4.03 mm, lens equivalent index = 1.418, Borja et al.)[14] surrounded by aqueous (n = 1.336) with back vertex power of 46.2 D and effective power of 43.5 D. To determine the off-axis lens power, a paraxial fan ray-trace was performed for an object point located at infinity and field angles ranging from 5° to 20° in 5° increments. The results are summarized in Table 4. The radius of curvature of the corresponding image field calculated using the same method as for the experiments is -9.2 mm. The values for peripheral defocus and field curvature obtained on the simulated lens were similar to the average values measured experimentally (shown in Table 2). These results suggest that the peripheral defocus of the cynomolgus crystalline lens could be modeled using a homogeneous lens with an index equal to the equivalent index measured on-axis. This finding is in agreement with previously published work on monkey lenses that suggest that young monkey lenses may not have a substantial refractive index gradient.[28,29]

There is evidence that the crystalline lens is not rotationally symmetric, and that aberrations vary along different meridians.[30] It is also possible that the lens stretcher may induce unexpected high-order aberrations in the lens due to non-uniformity with stretching. These effects could not be assessed with the version of the software used in the present study, which enabled measurements only in a single meridian. However, the LRT-OCT system is capable of acquiring 3D OCT images of the ex vivo lenses and has been upgraded to enable ray trace measurements along multiple meridians of the lens (raster pattern). Using custom software written in MATLAB, the LRT recorded spot patterns can be used to calculate the Zernike wavefront coefficients of the lens using a least-squares curve fitting algorithm.[31] Future applications of this system will focus on obtaining raster ray trace data to measure the 2D wavefront aberration maps of the crystalline lens, and exploring how aberrations of the lens vary along different meridians. The system may also be used to acquire off-axis 3D OCT images of the crystalline lens to reconstruct the lens gradient refractive index (Mohamed, et al. *IOVS* 2017;58:ARVO E-Abstract 2715). Furthermore, the experimental data on lens peripheral defocus measured with this system could be used to model the peripheral defocus of the whole eye.

Table 3. Relative Peripheral Lens Power (D), Corresponding to Peripheral – Central, for the Delivery Angles: ±20°, ±15°, ±10°, ±5°, 0°

		Relative Peripheral Power (Peripheral − Central) Unstretched Lens, D								
Eye No.	**Age, y**	**−20°**	**−15°**	**−10°**	**−5°**	**0°**	**5°**	**10°**	**15°**	**20°**
1 OD	3.8	NA	9.4	2.2	0.5†	0.0	1.8†	3.1	7.4	12.2
2 OD	5.7	12.3	6.9	3.1	1.1†	0.0	0.3†	2.3	4.8	10.6
3 OD	6.3	11.5	11.0	−3.7	1.6	0.0	−0.7	−3.7	1.8	11.5
3 OS*	6.3	12.8	5.4	3.5	1.5	0.0	0.9	2.9	5.0	10.0
4 OD*	6.8	8.4	4.5	6.1	−2.8	0.0	−1.2	−0.5	4.7	10.0
4 OS	6.8	9.3	7.3	0.9	−0.4	0.0	0.3	1.7	6.8	11.8
5 OD	7.8	9.6	4.8	2.3	2.2	0.0	0.0	2.9	4.8	11.1
6 OD	8.4	13.2	6.1	−0.4	0.3†	0.0	−3.3†	2.5	3.9	7.9
7 OS	8.5	11.2	5.5	2.0	1.9	0.0	2.2	5.3	8.7	11.6
8 OD	9.2	9.7	6.4	2.8	0.2†	0.0	0.0†	1.5	4.2	11.1
9 OD	10.6	10.6	5.5	0.1	0.5	0.0	1.2	1.9	6.7	9.1
9 OS*	10.6	10.7	5.5	2.6	1.1†	0.0	4.5†	4.7	6.9	9.2
10 OD	12.4	8.3	4.3	2.5	−0.3†	0.0	0.9†	1.6	4.1	11.6
11 OD*	12.4	8.3	0.2	−1.8	1.3	0.0	−0.3	−1.9	1.2	6.5
11 OS	12.4	9.2	6.0	0.5	−1.2	0.0	−0.2	0.9	1.9	8.7
Average		10.5	6.7	1.1	0.6	0.0	0.2	1.8	5.0	10.7
SD		1.5	2.0	2.0	1.0	0.0	1.5	2.2	2.2	1.4
		Relative Peripheral Power (Peripheral − Central) Stretched Lens, D								
Eye No.	**Age, y**	**−20°**	**−15°**	**−10°**	**−5°**	**0°**	**5°**	**10°**	**15°**	**20°**
1 OD	3.8	7.6	5.5	2.3	1.4†	0.0	0.2†	2.9	6.6	8.4
2 OD	5.7	9.8	5.8	2.7	1.4†	0.0	0.3†	2.2	3.8	8.0
3 OD	6.3	7.2	1.0	−1.9	−1.5	0.0	−1.6	3.3	3.9	5.8
3 OS*	6.3	9.0	4.3	1.1	−1.2	0.0	1.9	1.8	3.1	10.5
4 OD*	6.8	5.5	3.8	−0.4	−1.2	0.0	−1.9	0.9	4.3	5.6
4 OS	6.8	6.3	2.4	0.3	−1.5	0.0	−2.5	1.3	4.1	9.2
5 OD	7.8	8.1	4.5	1.7	−0.9	0.0	0.7	0.6	4.0	7.7
6 OD	8.4	8.4	1.5	−1.0	−0.8†	0.0	−2.7†	0.7	−1.5	7.6
7 OS	8.5	NA	3.4	3.5	−0.2	0.0	−0.7	1.5	5.5	10.0
8 OD	9.2	6.7	4.8	2.0	0.5†	0.0	1.2†	2.0	4.4	7.8
9 OD	10.6	6.3	1.9	2.0	−0.2	0.0	−0.2	−1.2	2.4	6.1
9 OS*	10.6	10.0	5.2	3.6	0.9†	0.0	0.4†	0.9	2.2	4.8
10 OD	12.4	4.6	1.3	−1.9	−2.6†	0.0	−3.1†	−1.2	0.4	4.1
11 OD*	12.4	7.6	5.5	2.0	−0.3	0.0	−0.6	1.1	2.6	5.9
11 OS	12.4	8.4	3.8	1.7	−0.5	0.0	0.2	1.7	4.5	7.7
Average		7.3	3.3	1.0	−0.4	0.0	−0.8	1.2	3.5	7.5
SD		1.5	1.7	1.9	1.2	0.0	1.5	1.5	2.3	1.6

Measurements were obtained for each cynomolgus monkey lens in the unstretched and stretched states.
* Eyes shown in the Table but were excluded for the statistical analysis.
† Lens power measurement corresponds to the ±4° delivery angle rather than ±5°.

In summary, using a new method for measuring the accommodative changes in crystalline lens off-axis power, the cynomolgus monkey lens was found to have a significant accommodation-dependent curvature of field. The monkey lens power was found to significantly increase peripherally with increasing delivery angle in the unstretched and stretched states, corresponding to myopic peripheral defocus. Moreover, the peripheral defocus of the lens was found to significantly increase with accommodation. This finding indicates that the lens contributes significantly to the peripheral defocus of the whole eye, which could have implications on near work and the development of myopia.

Table 4. Peripheral Defocus With Varying Field Angle Calculated for a Monkey Lens With a Homogeneous Refractive Index Modelled in OSLO

Field Angle	Peripheral Defocus, D
0°	0
5°	0.4
10°	1.6
15°	3.7
20°	6.8

Acknowledgments

The authors thank Keke Liu, Daniel Lopez, and Yue Yao for their assistance with data processing; Victor Hernandez and Juan Silgado for their machining expertise; and Yu-Cherng Channing Chang, Heather Durkee, Kelly Mote, Nicholas Nolan, and Nidhi Relhan for photographing the final system setup. The authors thank Heather Durkee and Ashik Mohamed for their assistance with the data acquisition and image processing. The authors would also like to thank James Geary; Waldo Diaz; Norma Kenyon, PhD; Dora Berman-Weinberg, PhD, of the Diabetes Research Institute; and Julia Zaias, PhD, of the Division of Veterinary research at the University of Miami for scientific support.

Supported in part by National Institutes of Health Grants R01EY021834, F31EY021444 (Ruth L. Kirschstein National Re-

search Service Award Individual Pre-doctoral Fellowship; BMH); Center Grant P30EY14801; Australian Government Cooperative Research Centre Scheme (Vision CRC); Florida Lions Eye Bank; Karl R. Olsen and Martha E. Hildebrandt; Raksha Urs and Aaron Furtado; an unrestricted grant from Research to Prevent Blindness; and the Henri and Flore Lesieur Foundation (JMP).

Disclosure: **B. Maceo Heilman**, None; **F. Manns**, None; **M. Ruggeri**, None; **A. Ho**, None; **A. Gonzalez**, None; **C. Rowaan**, None; **A. Bernal**, Bioniko Consulting LLC (I); **E. Arrieta**, None; **J.-M. Parel**, None

References

1. Ferree C, Rand G, Hardy C. Refraction for the peripheral field of vision. *Arch Ophthalmol*. 1931;5:717–731.
2. Smith EL III, Kee CS, Ramamirtham R, Qiao-Grider Y, Hung LF. Peripheral vision can influence eye growth and refractive development in infant monkeys. *Invest Ophthalmol Vis Sci*. 2005;46:3965–3972.
3. Smith EL III, Hung LF, Huang J. Relative peripheral hyperopic defocus alters central refractive development in infant monkeys. *Vision Res*. 2009;49:2386–2392.
4. Smith EL III. Prentice Award Lecture 2010: a case for peripheral optical treatment strategies for myopia. *Optom Vis Sci*. 2011;88:1029–1044.
5. Seidemann A, Schaeffel F, Guirao A, Lopez-Gil N, Artal P. Peripheral refractive errors in myopic emmetropic, and hyperopic young subjects. *J Opt Soc Am A*. 2002;19:2363–2373.
6. Wallman J, Winawer J. Homeostasis of eye growth and the question of myopia. *Neuron*. 2004;43:447–468.
7. Sankaridurg P, Holden B, Smith EL III, et al. Decrease in rate of myopia progression with a contact lens designed to reduce relative peripheral hyperopia: one-year results. *Invest Ophthalmol Vis Sci*. 2011;52:9362–9367.
8. Atchison DA, Li S-M, Li H, et al. Relative peripheral hyperopia does not predict development and progression of myopia in children. *Invest Ophthalmol Vis Sci*. 2015;56:6162–6170.
9. Mutti DO, Sinnott LT, Mitchell GL, et al. Relative peripheral refractive error and the risk of onset and progression of myopia in children. *Invest Ophthalmol Vis Sci*. 2011;52:199–205.
10. Sng CC, Lin XY, Gazzard G, et al. Peripheral refraction and refractive error in Singapore Chinese children. *Invest Ophthalmol Vis Sci*. 2011;52:1181–1190.
11. Atchison DA, Pritchard N, White SD, Griffiths AM. Influence of age on peripheral refraction. *Vision Res*. 2005;45:715–720.
12. Glasser A, Campbell MCW. Presbyopia and the optical changes in the human crystalline lens with age. *Vision Res*. 1998;38:209–229.
13. Artal P, Berrio E, Guirao A, Piers P. Contribution of the cornea and internal surfaces to the change of ocular aberrations with age. *J Opt Soc Am A*. 2002;19:137–143.
14. Borja D, Manns F, Ho A, et al. Refractive power and biometric properties of the nonhuman primate isolated crystalline lens. *Invest Ophthalmol Vis Sci*. 2010;51:2118–2125.
15. Birkenfeld J, de Castro A, Marcos S. Contribution of shape and gradient refractive index to the spherical aberration of isolated human lenses. *Invest Ophthalmol Vis Sci*. 2014;55:2599–2607.
16. Maceo Heilman B, Manns F, de Castro A, et al. Changes in monkey crystalline lens spherical aberration during simulated accommodation in a lens stretcher. *Invest Ophthalmol Vis Sci*. 2015;56:1743–1750.
17. Whatham A, Zimmerman F, Martinez A, et al. Influence of accommodation on off-axis refractive errors in myopic eyes. *J Vis*. 2009;9(3):14.
18. Lundstrom L, Mira-Agudelo A, Artal P. Peripheral optical errors and their change with accommodation differ between emmetropic and myopic eyes. *J Vis*. 2009;9(6):17.
19. Mathur A, Atchison DA, Charman WN. Effect of accommodation on peripheral ocular aberrations. *J Vis*. 2009;9(12):20.
20. Liu T, Sreenivasan V, Thibos LN. Uniformity of accommodation across the visual field. *J Vis*. 2016;16(3):6.
21. Roorda A, Glasser A. Wave aberrations of the isolated crystalline lens. *J Vis*. 2004;4(4):1.
22. De Castro A, Birkenfeld J, Maceo B, et al. Influence of shape and gradient refractive index in the accommodative changes of spherical aberration in nonhuman primate crystalline lenses. *Invest Ophthalmol Vis Sci*. 2013;54:6197–6207.
23. Nankivil D, Maceo Heilman B, Durkee H, et al. The zonules selectively alter the shape of the lens during accommodation based on the location of their anchorage points. *Invest Ophthalmol Vis Sci*. 2015;56:1751–1760.
24. Ruggeri M, Uhlhorn SR, De Freitas C, Ho A, Manns F, Parel JM. Imaging and full-length biometry of the eye during accommodation using spectral domain OCT with an optical switch. *Biomed Opt Express*. 2012;3:1506–1520.
25. Armstrong RA. Statistical guidelines for the analysis of data obtained from one or both eyes. *Ophthalmic Physiol Opt*. 2013;33:7–14.
26. Born M, Wolf E. *Principles of Optics. Electromagnetic Theory of Propagation, Interference and Diffraction of Light*. 7th ed. Cambridge: Cambridge University Press. 1980:228–260.
27. Escudero-Sanz I, Navarro R. Off-axis aberrations of a wide-angle schematic eye model. *J Opt Soc Am A*. 1999;16:1881–1891.
28. Augusteyn RC, Maceo Heilman B, Ho A, Parel J-M. Nonhuman primate ocular biometry. *Invest Ophthalmol Vis Sci*. 2016;57:105–114.
29. Maceo BM, Manns F, Borja D, et al. Contribution of the crystalline lens gradient refractive index to the accommodation amplitude in non-human primates: In vitro studies. *J Vis*. 2011;11(13):23.
30. Sun M, Birkenfeld J, de Castro A, Ortiz S, Marcos S. OCT 3-D surface topography of isolated human crystalline lenses. *Biomed Opt Express*. 2014;5:3547–3561.
31. Yao Y. *Zernike Wavefront Reconstruction of In Vitro Crystalline Lenses From Laser Ray Tracing Spot Patterns* [master's thesis]. Coral Gables, FL: University of Miami; 2016.

Investigative Ophthalmology & Visual Science